Nano Research

Open Access

Research Article

Unipolar modulated volatile memristor: Achieving multi-scale plasticity, associative learning, and dynamic reservoir computing

Jie Lu[1,§], Kexiang Wang[1,§], Haoyu Li[1], Zeyang Xiang[1], Junxiu Zhou[1], Yun Wen[1], Junyu Wang[1], Xinyu Cao[1], Weitian Xun[1], Yegang Lu[1], and Ran Jiang[1,2] ✉

[1] *Faculty of Electrical Engineering and Computer Science, Ningbo University, Ningbo 315211, China*
[2] *Qingdao Tailao Technology Co., Ltd, Qingdao 266101, China*
§ *Jie Lu and Kexiang Wang contributed equally to this work.*

Cite this article: *Nano Research*, **2026**, *19*, 94908641. https://doi.org/10.26599/NR.2026.94908641

ABSTRACT: The von Neumann architecture is nearing its physical limits regarding energy efficiency and parallelism. Consequently, brain-inspired computing hardware is viewed as a crucial solution to address these limitations. This research presents a volatile memristor featuring an Ag/Al_2O_3/Ti/Al_2O_3/ITO configuration for applications in brain-inspired computing. The device demonstrates conductivity modulation under unipolar pulses, attributed to the dynamic competition between electric field-driven drift and heat-induced diffusion, governed by the oxygen vacancy reservoir formed by the *in situ* oxidized Ti interlayer. The device exhibits multi-scale plasticity, encompassing short-term facilitation (STF), paired-pulse facilitation (PPF), and dependence on frequency and duty cycle. Switching between potentiation and depression can be achieved under the same polarity by tuning the strength of forward stimulation (amplitude, width, or interval). The device emulates the classical conditioned reflex of the spotted butterfly and establishes a dynamic reservoir, attaining accuracies of 97.05% and 83.22% in the MNIST and Fashion-MNIST image recognition tasks, with normalized mean square errors (NMSE) for the two second-order nonlinear system tasks of approximately 0.123 and 0.108, respectively. This study outlines a methodology for fabricating unipolar volatile memristors, thus enhancing the understanding of brain-inspired computing hardware.

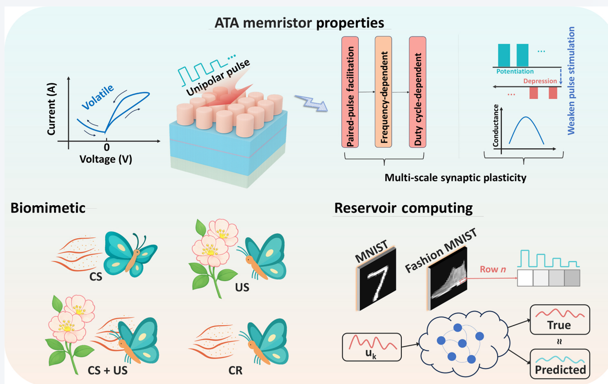

KEYWORDS: volatile memristors, electrothermal coupling, multi-scale plasticity, associative learning, reservoir computing

1 Introduction

With the traditional von Neumann architecture nearing its physical limits in energy efficiency and parallelism, brain-inspired computing, which emulates the highly parallel, event-driven, and asynchronous operations of biological neural networks at the hardware level, is regarded as a promising solution to address these limitations [1–3].

In biological neural networks, synapses produce postsynaptic potentials (PSPs) within a millisecond timeframe via the opening and closing of Na^+ and K^+ channels on the membrane, initiated by neurotransmitters released from presynaptic neurons, facilitating information transfer between neurons [4]. Synaptic weights are regulated dynamically via multi-scale plasticity mechanisms, including short-term facilitation (STF) and short-term depression (STD), as well as more persistent forms of potentiation and depression [5]. The dynamic modulation mechanisms enable organisms to engage in associative learning behaviors, exemplified by classical conditioning, through the pairing of unconditioned stimuli (US) with conditioned stimuli (CS) [6]. Furthermore, the temporal decay and summation of postsynaptic potentials translate continuous inputs into high-dimensional, reusable dynamical state spaces, creating an inherent "dynamic reservoir" for the real-time processing of complex rhythmic, linguistic, or motor sequence information [7]. These biological mechanisms have already been leveraged to build edge-intelligent systems that process temporally structured streams (such as robotics control, always-on IoT sensing, and real-time signal processing) [8] and have motivated neuromorphic hardware (e.g., complementary metal-oxide-

Received: October 27, 2025; **Revised:** February 19, 2026
Accepted: March 16, 2026

✉Address correspondence to jiangran@nbu.edu.cn

semiconductor (CMOS) spiking processors, ferroelectric transistors (FeFETs), spintronic magnetic tunnel junctions (MTJs), and photonic neuromorphic circuits) [9, 10]. However, many implementations still fall short of faithfully capturing the full breadth of these dynamics. To develop efficient brain-inspired computing hardware, it is essential to equip artificial synapses with multi-scale dynamic plasticity and adaptive balancing capabilities that align with those of biological synapses [11–13].

Recently, memristors have been identified as key candidates for simulating synaptic functions due to their low power consumption, high switching speed, and potential for three-dimensional integration [14–20]. Despite the ability of mainstream non-volatile memristors (NVMs) to stably store multi-level weights, they do not possess spontaneous decay capabilities and necessitate additional reset operations after data is written. Volatile memristors (VVMs) inherently demonstrate a self-recovery window, showcasing dynamic synaptic characteristics including short-term facilitation/short-term depression, frequency-dependent gain, and threshold detection, all without the necessity for supplementary "erase" operation [21, 22]. Among volatile devices, Mott transition materials (e.g., VO_2, NbO_2) [23–25] typically function as binary threshold switches driven by insulator-metal transitions. While effective for simulating spiking neurons, their abrupt switching characteristics limit their capability to emulate the continuous, analog weight modulation required for complex synaptic dynamics. Meanwhile, oxygen vacancy-based counterparts (e.g., WO_x) [26, 27] typically rely on pulses of opposite polarities (positive and negative) to achieve potentiation and depression, respectively. This diverges from biological rules, where plasticity reflects amplitude- and timing-dependent induction (often mediated by frequency and Ca^{2+} thresholds). This mismatch motivates architectures enabling volatility-mediated, unipolar modulation to bridge the gap between device physics and biological realism.

Trilayer oxide stacks have emerged as a robust architecture for controllable resistive switching. By combining a wide-bandgap interlayer (e.g., Al_2O_3) with a redox-active oxide (e.g., HfO_x or TiO_x), the stack geometrically and energetically confines ion/defect transport, thereby stabilizing multilevel analog conductance and reducing device-to-device variability through barrier engineering. Representative $HfO_2/Al_2O_3/HfO_2$ tri-layers on indium tin oxide (ITO) exhibit reliable, continuously tunable states governed by compliance current and reset-stop voltage, highlighting how the Al_2O_3 interlayer regulates filament formation/dissolution dynamics [28]. Physics-based analyses in $HfO_x/Al_2O_3/TiO_2$ stacks further elucidate the role of Al_2O_3 as a field/defect modulator that improves endurance and uniformity [29]. More recently, filament-free bulk-switching tri-layers achieved up to ~ 10^2 discernible levels without program-verify loops [30], underscoring the broader advantages of trilayer stacks for neuromorphic accuracy.

Accordingly, this study presents the development of a volatile memristor characterized by an $Ag/Al_2O_3/Ti/Al_2O_3/ITO$ structure, henceforth termed the ATA memristor. A 5 nm Ti interlayer undergoes *in-situ* oxidation to form TiO_x at the Al_2O_3/Ti interface, yielding an $Al_2O_3/TiO_x/Al_2O_3$ trilayer with symmetric Al_2O_3 barriers. By leveraging the TiO_x layer as a thermodynamic vacancy reservoir [31] and exploiting electrothermal coupling to regulate the drift-diffusion kinetics, the device facilitates the reversible aggregation and dispersion of oxygen vacancies [32, 33], thereby achieving multi-scale plasticity under unipolar pulses. The ATA memristor demonstrates STF/paired-pulse facilitation (PPF), spontaneous decay, and frequency- and duty-cycle-dependent weight changes on the millisecond-to-second scale. Additionally, it enables switching between potentiation and depression on the same platform by tuning the strength of same-polarity stimulation (e.g., pulse amplitude/width/interval as configured). We simulated the associative learning process of classical conditioned reflex using the ATA memristor and constructed a dynamic reservoir within the integrated *LTspice* and *Matlab* simulation framework. Accuracies of 97.05% and 83.22% were attained in image recognition tasks on MNIST and Fashion MNIST, respectively. The normalized mean square error (NMSE) in two second-order nonlinear system prediction tasks was approximately 0.123 and 0.108, respectively, indicating its efficacy in handling temporal tasks. This study presents a comprehensive new paradigm for developing volatile memristors, covering material design, mechanisms, and applications.

2 Results and discussion

2.1 Structure and characterization of the ATA memristor

Figure 1(a) depicts a typical biological synapse, wherein excitatory or inhibitory neuro-transmitters released from the presynaptic neuron interact with postsynaptic receptors. This interaction leads to the accumulation and integration of signals, which ultimately influences the excitation or inhibition of the postsynaptic neuron [34]. This study presents the fabrication of an artificial synaptic device utilizing an $Ag/Al_2O_3/Ti/Al_2O_3/ITO$ architecture on an ITO-coated glass substrate (Fig. 1(b)). Comprehensive procedures are outlined in the Experimental section.

Figure 1(c) illustrates the cross-section obtained through focused ion beam (FIB) milling. High-angle annular dark-field scanning transmission electron microscopy (HAADF-STEM) in conjunction with energy-dispersive X-ray spectroscopy (EDS) clearly delineates the five-layer structure of $Ag/Al_2O_3/Ti/Al_2O_3/ITO$ from top to bottom. Both Al_2O_3 layers have a thickness of 50 nm, while the interposed Ti layer measures approximately 5 nm, exhibiting sharp and uniform interfaces throughout. The high-resolution transmission electron microscopy (HRTEM) inset (red box) focusing on the $Al_2O_3/Ti/Al_2O_3$ region indicates that Al_2O_3 is amorphous, while the Ti layer exhibits no distinct lattice fringes, suggesting a nanocrystalline state. The EDS maps reveal a significant oxygen signal correlated with the Ti region (refer to Note S1 in the Electronic Supplementary Material (ESM)), which is ascribed to the high oxygen affinity of Ti and its partial interfacial oxidation to TiO_x due to residual oxygen presence [35–39]. A minor indium signal is detected within the top Ag electrode, attributed to the overlap of Ag-L and In-L emission lines rather than actual elemental diffusion.

Figure 1(d) presents the X-ray photoelectron spectroscopy (XPS) analysis of the $Al_2O_3/Ti/Al_2O_3$ switching layer, highlighting the Ti 2p, Al 2p, and O 1s peaks. High-resolution Ti 2p spectra were deconvoluted into three constrained spin-orbit doublets [40] assigned to metallic Ti^0, TiO (Ti^{2+}), and TiO_2 (Ti^{4+}). The $2p_{3/2}$ components are centered at 454.1, 456.2, and 458.2 eV; their $2p_{1/2}$ counterparts were constrained to lie 5.6–6.1 eV higher (459.8, 462.3, and 464.2 eV), with a 2:1 area ratio ($2p_{3/2}$:$2p_{1/2}$) and equal full width half maximum (FWHM) using Voigt line shapes and a Shirley background (C 1s = 284.8 eV). The coexistence of metallic and oxidized states indicates *in-situ* oxidation of the Ti interlayer,

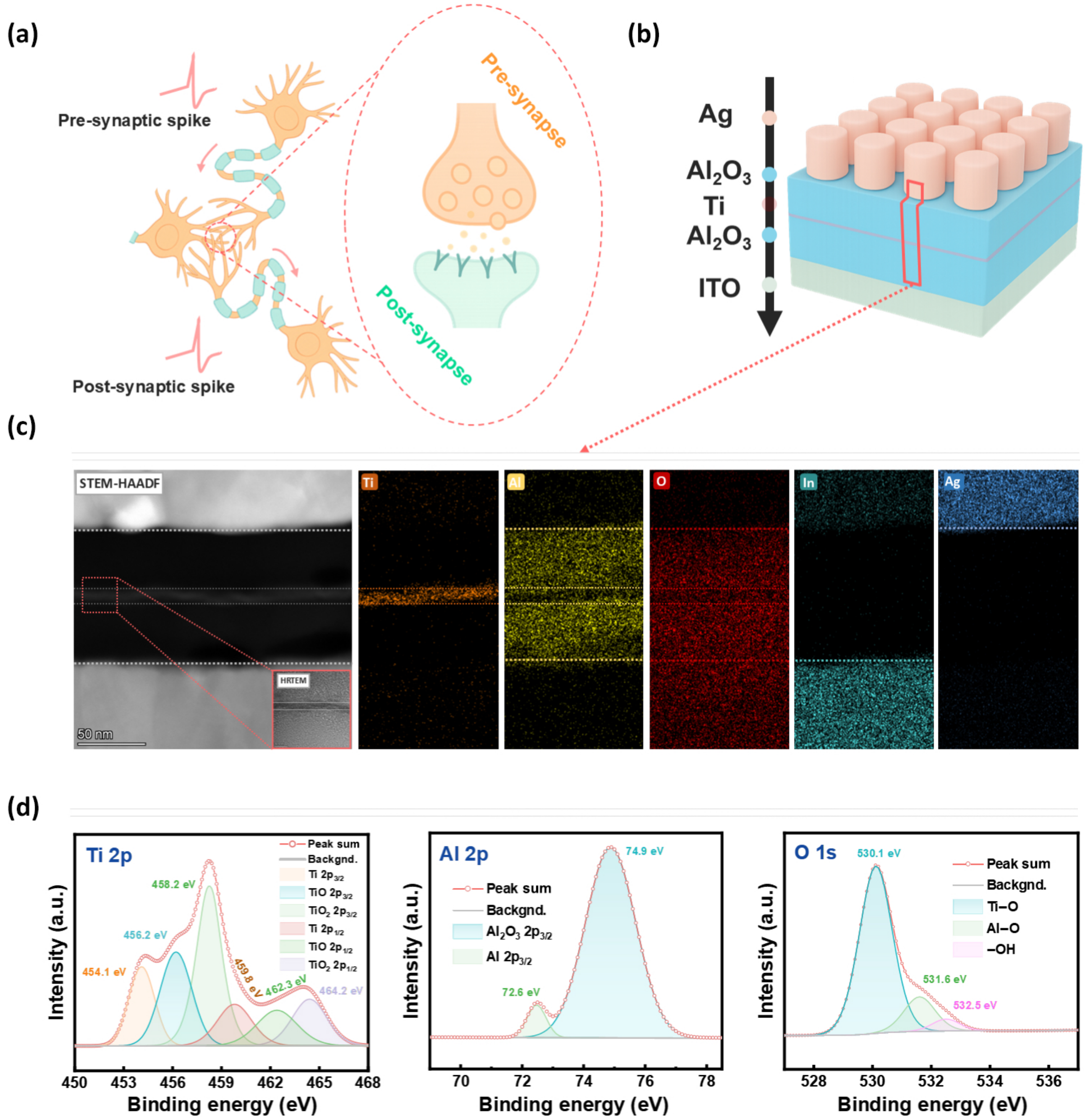

Figure 1 Device structure and characterization. (a) Schematic of a neuron and synapse. (b) Schematic of the Ag/Al_2O_3/Ti/Al_2O_3/ITO (ATA) memristor. (c) STEM-HAADF image of the device cross-section sample prepared using FIB and its corresponding EDS elemental distribution map. The inset in the left HAADF image shows the local HRTEM image of the Al_2O_3/Ti/Al_2O_3 region (red box). (d) XPS of the Al_2O_3/Ti/Al_2O_3 region, showing the Ti 2p, Al 2p, and O 1s characteristic peaks.

yielding sub-stoichiometric TiO_x at the interface. The Al 2p spectrum exhibits a dominant Al_2O_3 peak at 74.9 eV with a weaker shoulder near 72.6 eV, consistent with oxygen-deficient alumina. The O 1s envelope was deconvoluted into components at 530.1 eV (lattice Ti–O in TiO_x), 531.6 eV (Al–O in Al_2O_3), and a minor high-BE shoulder at 532.5 eV (surface –OH), confirming contributions from both TiO_x and Al_2O_3.

2.2 Basic electrical properties

Figure 2(a) presents the comprehensive I–V characteristics of the ATA memristor, which is subjected to bidirectional scanning under a compliance current of 10 mA. The ATA device demonstrates threshold switching (TS) characteristics. The scan initiates at 0 V and progresses in the forward direction. At a voltage of 0.7 V, the current experiences a significant alteration, resulting in the transition of the device from the high-resistance state (HRS) to the low-resistance state (LRS), a phenomenon known as Set. Within the same forward voltage range, the bias decreases, and due to the electric field–Joule heating coupling effect (as outlined in Section 2.3), the device transitions from LRS to HRS, a process known as Reset. Under negative bias (–0.5 to 0 V), the current is maintained below 1 mA, demonstrating a rectifying characteristic with a rectification ratio of approximately 10. The observed behavior is due to the asymmetric Schottky barrier present at the Ag/Al_2O_3 and Al_2O_3/ITO interfaces, which restricts electron flow when a negative bias is applied [41].

We conducted a fitting analysis of the I–V characteristics for both HRS and LRS to further investigate the conductive mechanism of the device (refer to Fig. S2 in the ESM). The findings indicate that within the low voltage range, the device adheres to the Schottky emission mechanism. Conversely, in the high voltage range, the HRS demonstrates typical space-charge-limited current (SCLC)

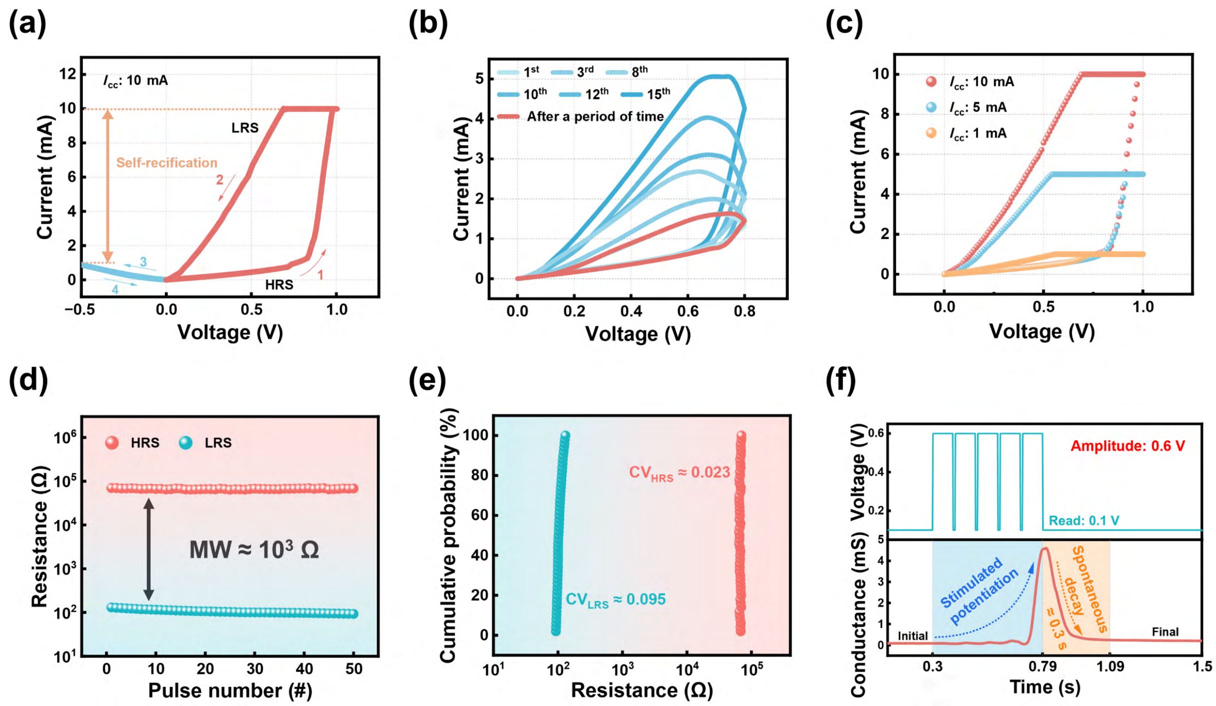

Figure 2 Basic electrical properties. (a) *I*–*V* curve of the ATA memristor. (b) Progressive potentiation and self-recovery characteristics of the memristor under continuous forward *I*–*V* scanning. (c) Forward *I*–*V* curves under different compliance currents (1, 5, 10 mA). (d) HRS and LRS of the ATA memristor under two sets of different forward pulse conditions. (e) Cumulative probability (C.P.) distribution of HRS and LRS values extracted from (d). (f) "Stimulated potentiation and spontaneous decay" process of the ATA memristor conductance under five pulse stimulations (amplitude: 0.6 V).

behavior, highlighting the conductive properties influenced by the interaction between the interface barrier and carrier injection (refer to Note S2 in the ESM for a detailed analysis).

In continuous forward *I*–*V* scanning (0–0.8 V), the conductivity window of the ATA memristor gradually increases, demonstrating a progressive potentiation behavior, after a period of time (≈ 10 s), while tested again, the window returns to its initial level (Fig. 2(b)). This phenomenon indicates that the device is a typical volatile memristor. Furthermore, the device-to-device uniformity was verified by testing multiple randomly selected cells, as detailed in Note S3 in the ESM. Figure 2(c) illustrates the *I*–*V* characteristics at varying compliance currents (1, 5, 10 mA), resulting in three distinct current platforms associated with different conductivity values. This indicates the potential for multi-level conductivity storage through the modulation of compliance current [42].

To assess conductivity modulation and storage through full forward pulses, we implemented 50 cycles of high-amplitude forward pulses (amplitude: 0.7 V, width: 90 ms, interval: 10 ms) and 50 cycles of low-amplitude forward pulses (amplitude: 0.3 V, width: 10 ms, interval: 10 ms) on the ATA memristor, yielding its LRS and HRS, as illustrated in Fig. 2(d). Both conditions demonstrated superior cycling stability and effective conductivity regulation. Figure 2(e) presents the cumulative probability distribution for the HRS and LRS obtained from the cyclic data illustrated in Fig. 2(d). The distribution ranges of HRS and LRS are distinctly separated. Further calculations reveal that the coefficient of variation (CV) for HRS and LRS are 0.023 and 0.095, respectively, suggesting that the ATA memristor exhibits strong state stability and discrimination margin under forward pulse modulation.

Figure 2(f) illustrates the process of conductivity potentiation and the subsequent spontaneous recovery behavior over time, stimulated by forward pulses with amplitudes of 0.6 V (5 pulses). The result demonstrates the characteristic behavior of "Stimulated potentiation and spontaneous decay" under continuous pulse stimulation, conductivity progressively increases, while in the absence of stimulation, conductivity spontaneously returns to its initial value within a time range of milliseconds to seconds (≈ 0.3 s). The "force–recovery" behavior parallels the short-term synaptic facilitation (STF) mechanism observed in biological synapses. Continuous neuronal excitation increases synaptic transmission efficiency, and following the cessation of stimulation, the synaptic response progressively returns to baseline levels within a brief timeframe, attributed to neurotransmitter reuptake and receptor desensitization [43, 44]. The ATA memristor demonstrates macroscopic dynamic characteristics akin to short-term synaptic plasticity, indicating its potential application in brain-inspired computing and synaptic modeling.

2.3 Mechanism of the ATA memristor

In light of the *I*–*V* characteristics of the ATA memristor (Fig. 2(a)) previously discussed, we undertook a comprehensive analysis of its underlying mechanism. The valence charge mechanism (VCM) theory posits that the conductive switching of the memristor is primarily due to the migration and accumulation of oxygen vacancies in response to the applied electric field. This process induces alterations in the local oxidation state of the material, ultimately resulting in the formation or rupture of conductive channels [45]. The movement of oxygen vacancies encompasses three main aspects: diffusion driven by thermal excitation, directional drift influenced by the electric field, and the formation and recombination of localized oxygen vacancies within the dielectric layer [46].

In the ATA device, the generation of such localized vacancies is governed by the strong oxygen affinity of the 5 nm titanium interlayer. Acting as an effective oxygen scavenger, the Ti layer extracts oxygen ions from the adjacent Al_2O_3 lattice. This spontaneous interfacial reaction simultaneously generates a high concentration of oxygen vacancies and transforms the metallic Ti into a non-stoichiometric TiO_x layer. Due to the lower vacancy formation energy in this defective oxide compared to the Al_2O_3 layer, the resulting TiO_x layer functions as a deep thermodynamic potential well (oxygen reservoir), effectively confining and accumulating these vacancies at the interface.

Based on this interfacial configuration, we analyzed the dynamic switching evolution as illustrated in Fig. 3(a). State 1 displays the initial equilibrium, where a dense vacancy reservoir is confined by the deep thermodynamic potential well (top panel) at the Ti/Al_2O_3 interface, coexisting with sparse intrinsic vacancies distributed within the bulk Al_2O_3. Upon reaching V_{Set}, the synergistic effect of the electric field and Joule heating lowers the effective migration barrier of the TiO_x layer (visualized as the curved potential well in the State 2 top panel). Consequently, the directional drift of these vacancies dominates over random thermal motion ($F_{drift} > F_{diffusion}$), facilitating the assembly of the conductive filament (in the bottom panel of State 2). Subsequently, the accumulation of oxygen vacancies leads to a surge in local current density, triggering intense Joule heating and massive random thermal diffusion. This isotropic diffusive force rapidly intensifies until it overwhelms the prevailing directional drift ($F_{diffusion} > F_{drift}$), driving oxygen vacancies to scatter stochastically into the surrounding bulk or be re-captured by the interfacial potential well. This redistribution leads to the rupture of the conductive filament and the restoration of the HRS (State 3).

To corroborate the proposed electro-thermal mechanism, we performed finite element simulations of the ATA memristor using COMSOL multiphysics (the detailed modeling process is outlined in Note S4 in the ESM). Specifically, we reconstructed the field distributions for the conductive path geometries in the LRS holding stage (State 2) and the reset trigger stage (State 3), as shown in Fig. 3(b). While the lower panels illustrate the dense oxygen vacancy accumulation within the filament region, the upper panels reveal the corresponding thermal consequences. Crucially, State 3 exhibits a distinct high-temperature hotspot that spatially aligns with the filament constriction. Consequently, this intense localized Joule heating emerges as the primary thermodynamic driver to amplify random thermal diffusion ($F_{diffusion} > F_{drift}$), thereby validating the heat-induced rupture mechanism.

It is also worth noting that despite the geometric symmetry of the dielectric stack, the asymmetric work functions of the top Ag and bottom ITO electrodes, along with potential interfacial physicochemical effects, likely induce an internal built-in field that further facilitates the unipolar modulation behavior. Within the limits of our measurements and modeling, the modulation mechanism observed here is plausibly attributed to the synergistic action of this electrode asymmetry, the reactive Ti interlayer (acting as a vacancy reservoir), and the Al_2O_3 dielectric layer (shaping the electrothermal profile). Given that literature reports indicate that analogous functional layers, such as oxygen-scavenging Ta interlayers, can similarly tune vacancy dynamics [47], this suggests that such functionalized heterostructures could serve as a potential design strategy for realizing unipolar volatile modulation in related material systems.

2.4 Brain-inspired synaptic characteristics

The essence of brain-inspired synaptic plasticity lies in the ability to simultaneously emulate biological synaptic behaviors, including short-term dynamics, frequency/duration and interval-dependent modulation, as well as multi-scale phenomena such as potentiation and depression, all within a unified device platform [48]. Two consecutive pulses were applied to the ATA memristor. With a pulse interval of 7 ms, the Joule heat from the initial pulse had not fully dissipated. This residual heat transiently lowers the activation barrier of the TiO_x reservoir (thermal gating), facilitating the injection of oxygen vacancies during the second pulse. This leads to an expansion of the conductive channel and a notable rise in current (Fig. 4(a)). Conversely, with an extended interval, the second pulse did not augment the conductive channel, resulting in a stable current (Fig. 4(b)). This interval-dependent potentiation phenomenon closely resembles PPF observed in biological synapses. The PPF index is characterized as

$$\mathrm{PPF} = (A_2 - A_1)/A_1 \times 100\% \qquad (1)$$

Figure 4(c) presents experimental data and fitting curves that

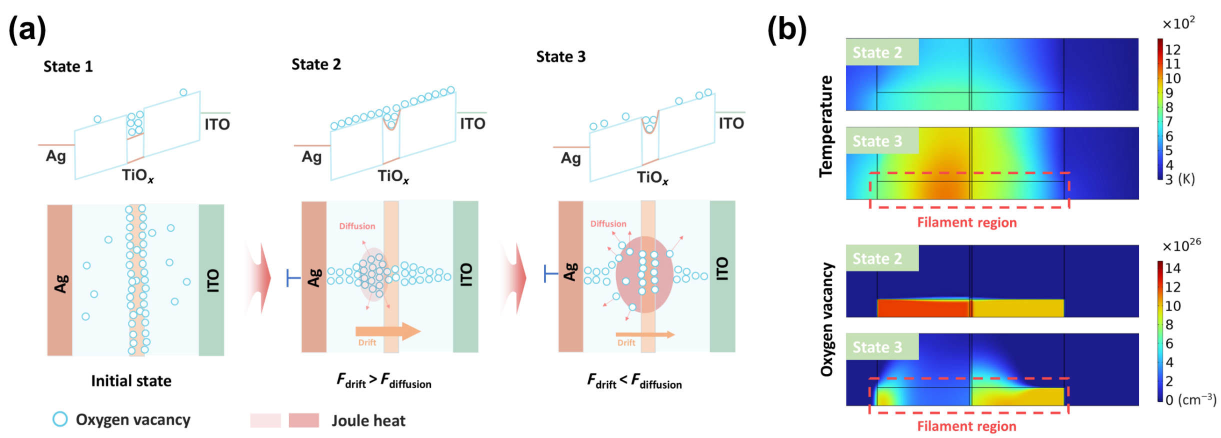

Figure 3 Mechanism of the ATA memristor. (a) Schematic illustration of the unipolar switching mechanism governed by the competition between electric field-induced drift and Joule heating-induced diffusion. The top panels present the energy band diagrams, highlighting the lowering of the effective migration barrier (potential well) of the TiO_x layer for oxygen vacancies due to electro-thermal coupling. The bottom panels depict the corresponding structural evolution of the conductive filament, driven by the interplay between directional drift flux (F_{drift}) and thermal diffusion flux ($F_{diffusion}$). (b) COMSOL multiphysics simulation of the ATA memristor. The upper and lower panels display the internal temperature and oxygen vacancy distributions, respectively. Note that the high-temperature hotspot in State 3 aligns perfectly with the filament region, supporting the thermal rupture mechanism.

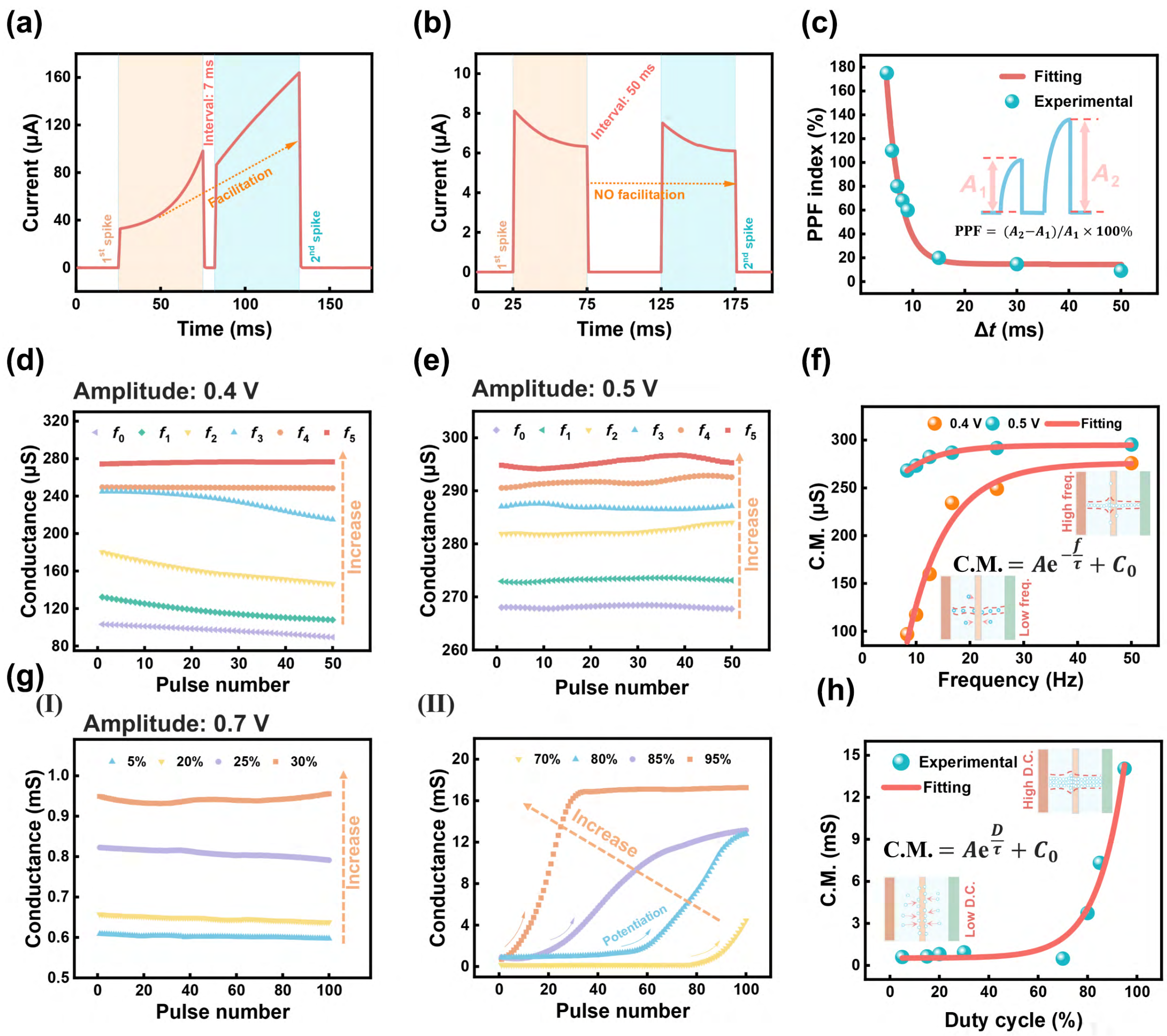

Figure 4 Brain-inspired synaptic characteristics. (a) and (b) Synaptic current under two consecutive pulses (pulse width: 50 ms, pulse interval: 7 and 50 ms). (c) Dependence of the PPF index on the pulse interval. (d) and (e) Conductance potentiation effect of the ATA memristor under six progressively increasing frequency pulse stimulations (f_0 = 8.33 Hz, f_1 = 10 Hz, f_2 = 12.5 Hz, f_3 = 16.67 Hz, f_4 = 25 Hz, f_5 = 50 Hz) at amplitudes of (d) 0.4 V and (e) 0.5 V. (f) Conductance mean values versus frequency, fitted with an exponential saturation model. Inset: schematics illustrating the gap-filling (percolation) mechanism that enhances filament connectivity at high frequencies. (g) Conductance evolution of the ATA memristor under different duty cycles (amplitude: 0.7 V). (I) Low duty cycles (5%, 20%, 25%, 30%) exhibit low conductance states with negligible variation. (II) High duty cycles (70%, 80%, 85%, 95%) induce a significant increase in conductance. (h) Nonlinear exponential growth of C.M. with increasing duty cycle. Inset: schematics depicting the transition from confinement within the TiO_x reservoir (low duty) to radial filament expansion (high duty).

illustrate the variation of the PPF index with pulse interval (Δt). As the interval increases, the PPF effect diminishes, suggesting that the ATA memristor is capable of simulating the short-term facilitation properties observed in biological synapses.

To further validate the device's capability in emulating biological synaptic plasticity, the conductance response was systematically evaluated by varying the pulse parameters. Initially, 50-cycle forward-pulse trains were applied at six increasing frequencies (8.33 to 50 Hz) under amplitudes of 0.4 and 0.5 V (Figs. 4(d) and 4(e)). The results reveal a clear frequency-dependent potentiation. This behavior aligns with the biological principle where higher presynaptic firing rates strengthen synaptic efficacy, whereas lower rates permit recovery and yield weaker potentiation [49, 50]. To quantify this dynamic evolution, the conductance mean (C.M.) was calculated and fitted using unified exponential models. As shown in Fig. 4(f), the C.M. gradually approaches a saturation limit with increasing frequencies. This behavior is well-described by the exponential saturation model

$$\mathrm{C.M.} = Ae^{-f/\tau} + C_0 \tag{2}$$

where f is the frequency, and τ represents the characteristic relaxation constant. This saturation behavior is attributed to the rate-dependent accumulation efficiency of oxygen vacancies. Under low-frequency stimulation, the aggregated vacancies are more easily recaptured by the TiO_x layer due to the sufficient relaxation time, resulting in a discontinuous conductive path. In contrast, high-frequency stimulation suppresses this relaxation, allowing vacancies to accumulate rapidly and bridge the filament gap (gap-filling process). Once the percolation threshold is reached and the path is fully connected, the potentiation effect naturally saturates (Fig. 4(f), inset).

However, frequency modulation represents a single-variable approach. In biological synapses, time scales are typically adjusted concurrently: Longer stimulation durations result in increased neurotransmitter release, while shorter recovery windows limit reuptake processes [33]. To emulate this "dual time-window" modulation, pulse trains with eight increasing duty cycles (5% to 95%) were applied at a fixed amplitude of 0.7 V. Figure 4(g) delineates two distinct modulation regimes. At low duty cycles (5%–30%, Fig. 4(g)(I)), the conductance remains low with negligible variation. In stark contrast, high duty cycles (70%–95%, Fig. 4(g)(II)) trigger a significant and abrupt potentiation. Figure 4(h) further elucidates this non-linearity, where the C.M. exhibits an exponential growth rather than saturation, as defined by

$$\text{C.M.} = Ae^{D/\tau} + C_0 \tag{3}$$

where D denotes the duty cycle. This drastic mathematical divergence implies a transition in the physical mechanism driven by the dual modulation of pulse width and interval. At low duty cycles (Fig. 4(h), left inset), the short pulse width provides insufficient drift force, while the long interval allows the TiO_x reservoir to effectively recapture vacancies, making the formation of a stable and effective conductive path difficult. Conversely, at high duty cycles (Fig. 4(h), right inset), the extended width generates Joule heat while the shortened interval suppresses relaxation. This synergistic effect triggers a positive feedback loop, driving the filament from a "confined" state to a "radial growth" state (lateral expansion), resulting in the observed exponential conductance surge.

Consequently, the conductance evolution in the ATA memristor is fundamentally governed by the dynamic competition between electric field-driven drift and thermally assisted diffusion. Based on this principle, we carefully designed a protocol using only unipolar positive pulses to emulate biological synaptic potentiation and depression processes (Fig. 5(a)). For potentiation, we applied a high-intensity train (50 pulses, 0.65 V, 50 ms width) with a short interval of 5 ms. This high-density, strong stimulation ensures the dominance of drift force over diffusion ($F_{\text{drift}} > F_{\text{diffusion}}$), while simultaneously accumulating a certain amount of Joule heat. As illustrated in Fig. 5(b) (left), the strong electric field drives the continuous accumulation of oxygen vacancies drawn from the TiO_x reservoir, leading to filament growth and a linear conductance increase (Fig. 5(c), blue region). In contrast, depression is achieved by leveraging the accumulated heat combined with weaker stimulation. We applied a pulse train with a lower amplitude (0.6 V, 30 ms width) and, crucially, a significantly extended interval of 40 ms. The residual Joule heat from the potentiation phase accelerates vacancy diffusion, while the weakened electric field and extended interval are insufficient to constrain them ($F_{\text{drift}} < F_{\text{diffusion}}$). Consequently, oxygen vacancies dissolve from the filament and diffuse back toward the TiO_x interface or surrounding matrix (Fig. 5(b), right), leading to filament rupture and a conductance decrease (Fig. 5(c), red region). To quantify the dynamics of this dissolution, we analyzed the synaptic weight change rate (W) during the depression phase (Fig. 5(d)), calculated as

$$\Delta W = (C_{2n} - C_1)/C_1 \times 100\% \tag{4}$$

where C_1 represents the maximum conductance after potentiation, and C_{2n} denotes the conductance value at the n^{th} depression pulse. The results reveal a distinct two-stage decay behavior. Phase I (Pulses 50–60) exhibits a rapid drop in weight. We attribute this to the high residual Joule heat, which temporarily boosts the diffusion coefficient. As the heat dissipates, the process transitions into Phase

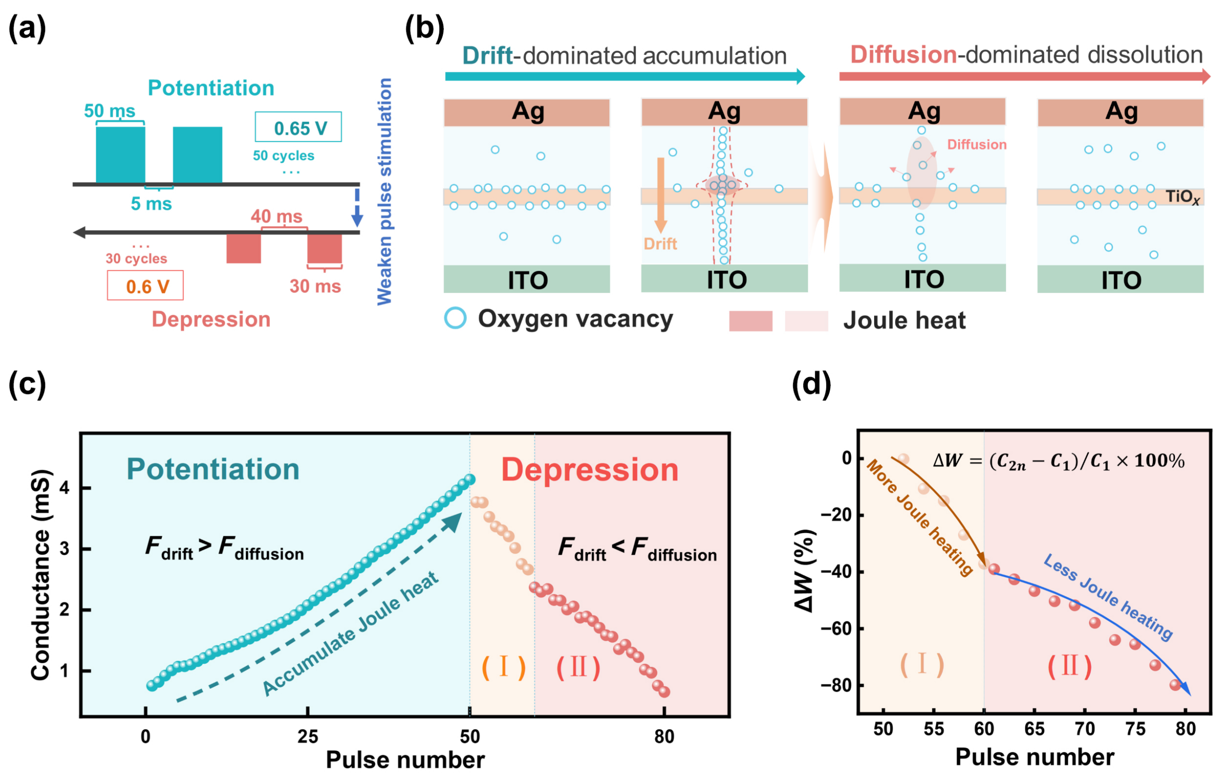

Figure 5 Emulation of biological synaptic potentiation and depression behaviors. (a) Schematic of the unipolar pulse stimulation protocol. A potentiation train (50 pulses, amplitude: 0.65 V, width: 50 ms, interval: 5 ms) is followed by a depression train (30 pulses, amplitude: 0.6 V, width: 30 ms, interval: 40 ms). (b) Schematic illustration of the filament evolution dynamics, where potentiation arises from drift-dominated accumulation (growth) and depression results from diffusion-dominated dissolution (rupture). (c) Potentiation and depression behaviors of the ATA memristor under unipolar pulse stimulation. The potentiation phase corresponds to the regime where the electric field drift force exceeds diffusion ($F_{\text{drift}} > F_{\text{diffusion}}$), while the depression phase is governed by diffusion dominance ($F_{\text{drift}} < F_{\text{diffusion}}$). (d) Analysis of the synaptic weight change rate (ΔW) during the depression process, highlighting the two-stage decay behavior ((I) and (II)) modulated by residual Joule heating.

II (Pulses 60–80), where the decay rate markedly slows, governed by pure concentration gradient-driven diffusion.

This precise manipulation of oxygen vacancy drift-diffusion kinetics enables the ATA memristor to replicate multi-scale biological plasticity, including PPF, frequency/duty-cycle dependence, and potentiation/depression, through a simplified unipolar driving scheme.

2.5 Biomimetic modeling of spotted butterfly associative behavior

Classical conditioning serves as the foundation for associative learning within the field of biology. The behavioral patterns have been thoroughly investigated across diverse organisms and are broadly utilized in the fields of biomimetic electronics and neuromorphic computing [51]. Figure 6(a) illustrates the four distinct stages of classical conditioned reflex in the spotted butterfly, identifying odor as the conditioned stimulus (CS) and nectar as the unconditioned stimulus (US). During Stage I, the butterfly shows minimal flight response to the isolated odor (CS). In Stage II, the nectar (US) stimulus initiates the foraging flight behavior of the butterfly. Following training with paired conditioned and unconditioned stimuli (Stage III), the butterfly associates the odor (CS) with the nectar (US), resulting in a distinct flight response. In Stage IV, the isolated odor (CS) is sufficient to induce flight behavior. The intensity (volatile concentration and chemical signal strength) and duration of both odor (CS) and nectar (US) stimuli are critical factors that directly influence the establishment of conditioned reflex behaviors and the formation of associative learning.

To simulate this process, we further verified the response characteristics of the ATA memristor to different voltage amplitudes and pulse widths. Figure 6(b) shows the current response under different voltage amplitudes (increasing from 0.5 to 0.7 V). As the amplitude increases, the current gradually crosses the threshold, exhibiting a noticeable potentiation effect. Figure 6(c) illustrates that under a fixed amplitude, by increasing the pulse width (from 50 to 400 ms), the current response similarly strengthens. This indicates that the ATA memristor can simulate the intensity and timing of odor and nectar stimuli by adjusting pulse amplitude and duration, effectively mimicking the classical conditioned reflex behavior of the spotted butterfly.

Specifically, we first configured the pulse width and interval to 50 μs. A 0.6 V pulse was designated as the conditioned stimulus (odor) and a 0.7 V pulse as the unconditioned stimulus (nectar), with a defined threshold current of 180 μA for the foraging flight response. As depicted in Fig. 6(d): (I) Application of the CS alone fails to trigger a response, as the current remains below the threshold. (II) Conversely, the US alone elicits a current significantly above the threshold, corresponding to the innate foraging behavior. (III) This stage encompasses both training and verification phases: Initially, alternating CS (0.6 V) and US (0.7 V) pulses are applied for training, where the robust response current is primarily driven by the US; subsequently, CS pulses (0.6 V) applied alone successfully elicit a supra-threshold response—in stark contrast to the null response in Stage (I)—thereby conclusively demonstrating the establishment of the conditioned reflex. Crucially, as shown in the final phase of Fig. 6(d), after the cessation of stimuli, the current spontaneously decays to the initial state (marked as "Forget..."). This demonstrates that the device possesses an intrinsic forgetting mechanism, faithfully mimicking the biological extinction process where a conditioned response fades over time without reinforcement.

Subsequently, to verify the timing-dependent plasticity, we maintained a fixed amplitude of 0.7 V while modulating the pulse duration (Fig. 6(e)). Pulses with a width of 10 μs (interval 10 μs) served as the CS, while those with a width of 90 μs (interval 10 μs) served as the US, with a response threshold of 90 μA. Consistent with the previous results, the CS and US applied individually in stages (I) and (II) elicited no response and a supra-threshold response, respectively. In stage (III), the paired stimulation successfully established the conditioned reflex, followed by a spontaneous decay of the synaptic weight upon stimulus withdrawal. These results confirm that by adjusting stimulation intensity (amplitude) and duration (width/interval), the ATA memristor can effectively emulate both the associative learning and the forgetting dynamics of the spotted butterfly.

2.6 Reservoir computing (RC)

RC serves as an effective computational framework for the analysis of time-series data, demonstrating particular efficacy in simulating dynamic and sequential learning tasks [52]. This method develops a multi-layered computational model that streamlines the training process through high-dimensional mapping of input data, thereby enabling the model to adjust to temporal changes and sequential information [11]. Two essential features are necessary for the implementation of this framework: the nonlinear current response of the memristor, which is vital for high-dimensional mapping, and its volatile characteristics, which guarantee that the input data in the reservoir is determined solely by the current input rather than previous input signals [26]. Figures 2(b) and 2(f) illustrate that the ATA memristor exhibits both characteristics, highlighting its adaptability and benefits in reservoir computing. This study presents a device model developed in *LTspice*, integrated with *MATLAB* for reservoir computing, successfully executing tasks including image recognition and the resolution of second-order nonlinear systems.

Figure 7(a) illustrates the RC-based models for image recognition of the MNIST and Fashion MNIST datasets. The 28 × 28 raw images were encoded into voltage pulses with amplitudes that varied according to their grayscale values; higher grayscale values corresponded to larger encoded voltage amplitudes. Two voltage pulse streams at different rates (with identical amplitude quantization) are delivered to the input layer sequentially, and then mapped to the reservoir implemented as an RRAM comprising 112 ATA memristors, yielding two temporal state trajectories. This configuration converts the data into a high-dimensional state space and facilitates the extraction of temporal features via nonlinear transformations. The readout layer classifies the fused reservoir states. These features are processed by a fully connected multilayer perceptron (MLP), which generates the final prediction using a rectified linear unit (ReLU) and SoftMax activation function.

In order to incorporate various states into the reservoir computing, we represented "1" with 0.7 V and "0" with 0 V. Figure 7(b) illustrates that sequential application of four-bit pulses resulted in 16 distinct reservoir states. The observed states demonstrate effective separation, suggesting that the reservoir is capable of producing diverse responses via different pulse patterns to facilitate computational and learning activities (for more information, see Note S5 in the ESM). For both the MNIST and Fashion MNIST datasets, we selected 50,000 training images and

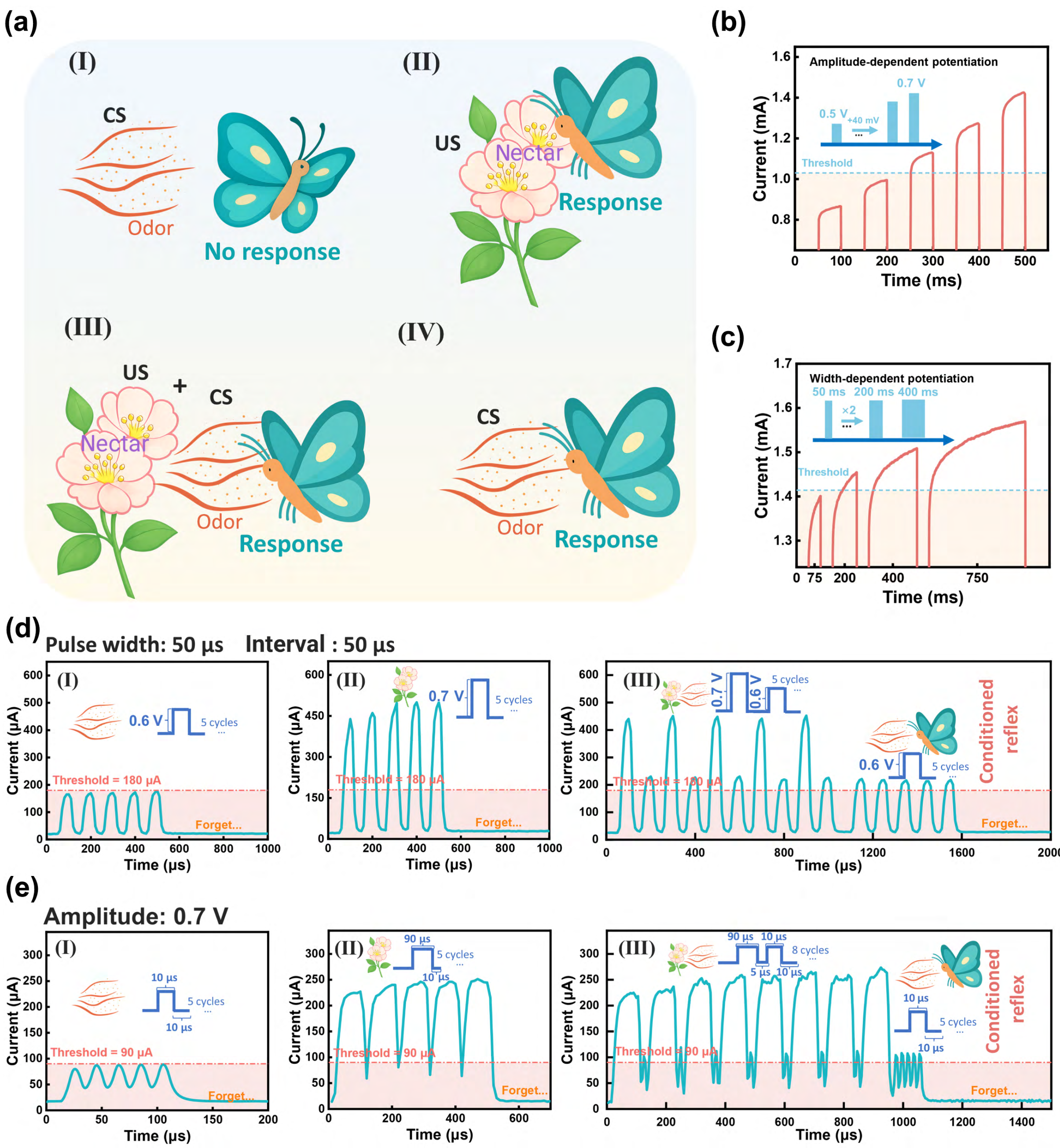

Figure 6 Biomimetic modeling of spotted butterfly associative behavior. (a) Schematic of classical conditioned reflex in the spotted butterfly, with odor and nectar as the CS and US, respectively. (b) Synaptic current potentiation with increasing stimulus intensity. (c) Synaptic current potentiation with increasing stimulus duration. (d) Simulation of classical conditioned reflex behavior: Under a fixed pulse width (50 μs) and interval (50 μs), pulses with 0.6 V amplitude simulate the CS, and pulses with 0.7 V amplitude simulate the US. The response threshold current is set to 180 μA (red dashed line). (I) Response current under CS stimulation alone (below threshold). (II) Response current under US stimulation alone (above threshold). (III) The associative learning process: after paired CS + US stimulation (training), the subsequent CS alone successfully triggers a response exceeding the threshold (conditioned reflex). (e) Similar simulation with a fixed voltage amplitude (0.7 V). The CS is defined by a pulse width of 10 μs, while the US corresponds to a pulse width of 90 μs. The response threshold current is 90 μA (red dashed line). (I)–(III) show the responses under CS alone, US alone, and the combined training-testing process, respectively, demonstrating the establishment of the conditioned reflex and the subsequent forgetting behavior.

10,000 test images for voltage pulse encoding. After reservoir computing, the data was fed into the MLP for training purposes. As illustrated in Fig. 7(c), the system attained peak accuracies of 97.05% for MNIST and 83.22% for Fashion-MNIST after 50 training epochs, with the detailed prediction distributions visualized in the confusion matrices of Figs. 7(d) and 7(e). Compared with the traditional MLP implemented using non-volatile memristors, the reservoir computing approach significantly reduces the number of devices required and optimizes the network structure due to the high-dimensional mapping (for details, see Note S6 in the ESM).

Nonlinear dynamic systems have significant engineering implications [53]. For instance, in robotics, force-regulated interaction tasks, such as surface following (polishing/deburring), peg-in-hole insertion, and compliant grasping, are dominated by

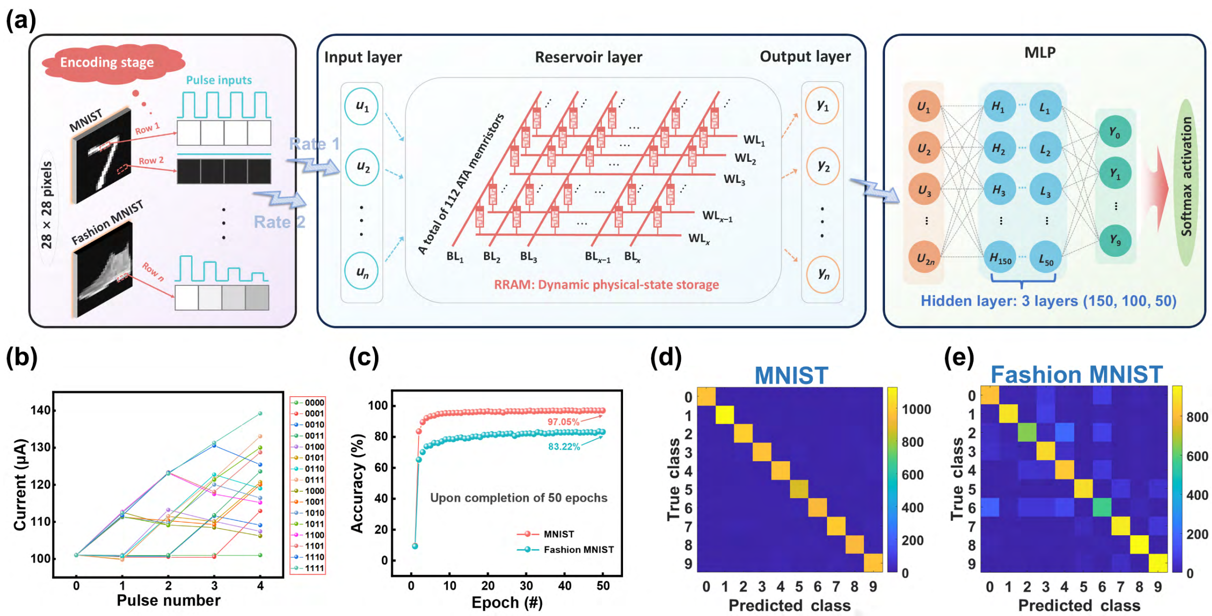

Figure 7 Image recognition task. (a) Schematic of image recognition using the MNIST and Fashion MNIST datasets, comprising three stages: image encoding, dynamic physical storage in RRAM, and multilayer perceptron. (b) Reservoir states of the ATA memristor for different 4-bit inputs. (c) Image recognition accuracy after 50 epochs of training. (d) Confusion matrix of the model on the MNIST dataset. (e) Confusion matrix of the model on the Fashion MNIST dataset.

the tool–environment contact and joint transmission, which together behave as a second-order nonlinear system with hysteretic restoring and damping terms [54]. Similar to biological signal processing, electroencephalography (EEG) event-related responses and rhythmic bursts are often captured by neural-mass formulations that embody second-order dynamics with nonlinear gain [55]. The primary benefit of reservoir computing is its capacity to analyze time-series data, facilitating the direct examination and forecasting of dynamic nonlinear systems [56]. To validate this capability, we further used the ATA memristor reservoir to solve a second-order dynamic nonlinear task, specifically selecting the following hysteretic second-order nonlinear system

$$y(k) = 0.5y(k-1) - 0.3y(k-2) + u(k) + 0.2y(k-1)u(k) - 0.1[y(k-1)]^2 + 0.1 \quad (5)$$

In practical applications, the relationship between $u(k)$ and $y(k)$ is typically indeterminate, with $y(k)$ being influenced not only by the current input $u(k)$ but also by preceding outputs $y(k–1)$ and $y(k–2)$. Conventional modeling and gradient backpropagation techniques face challenges in efficiently approximating dynamics in scenarios with limited samples and online conditions. Reservoir computing, characterized by its high-dimensional mapping and short-term memory capabilities, is particularly effective for addressing these tasks.

As shown in Fig. 8(a), we encoded the input signal into 19 different forms of voltage pulse sequences (9 of which have the same pulse width of 1 ms with varying intervals: 2, 3, 4, 5, 6, 8, 10, 15, and 20 ms; the remaining 10 sequences have the same pulse width and interval: 1, 2, 3, 4, 5, 6, 8, 10, 15, and 20 ms, which essentially modify the duty cycle and frequency for encoding). The voltage pulse vector was then input into the ATA memristor reservoir, where it was converted into a current readout using Ohm' s law. Similar to the MNIST image recognition task, the readout was used as high-dimensional features and input into an MLP. After training with linear regression, the predicted output values for the second-order nonlinear system were compared to the actual computed values.

Figure 8(b) shows the random signal input and the comparison between the actual output and predicted values during the training process, with the calculated NMSE being 0.092. Figure 8(c) presents the actual output and predicted values for two different random signal inputs during the testing process, with NMSE values of 0.123 (I) and 0.108 (II) (comparable to reported benchmarks for experimental reservoir computing systems [57, 58]), indicating that the predicted values closely match the actual values in both amplitude and phase, validating that the ATA memristor-based reservoir computing can accurately capture and predict complex second-order nonlinear dynamics.

3 Conclusion

The Ag/Al_2O_3/Ti/Al_2O_3/ITO volatile memristor proposed in this work leverages the synergistic interaction between the TiO_x vacancy reservoir and electrothermal-driven diffusion kinetics. Using unipolar pulses within a single device, it realizes a comprehensive set of synaptic behaviors that more closely reflect biological mechanisms (STF/PPF, frequency- and duty-cycle-dependent modulation, and same-polarity switching between potentiation and depression).

Building on this mechanism, the ATA memristor successfully mimicked the classical conditioned reflex of the spotted butterfly: by adjusting the pulse amplitude and width/interval, the "odor-nectar" stimuli were mapped into voltage sequences, completing associative learning and threshold decision-making within milliseconds. This demonstrates the generalization potential of the ATA memristor in simulating diverse biological behaviors.

Furthermore, we constructed a dynamic reservoir using the *LTspice* and *MATLAB* joint framework, utilizing the device's nonlinearity and self-recovery characteristics to achieve high-dimensional mapping and short-term memory. The model achieved high accuracy in image recognition tasks and low-error

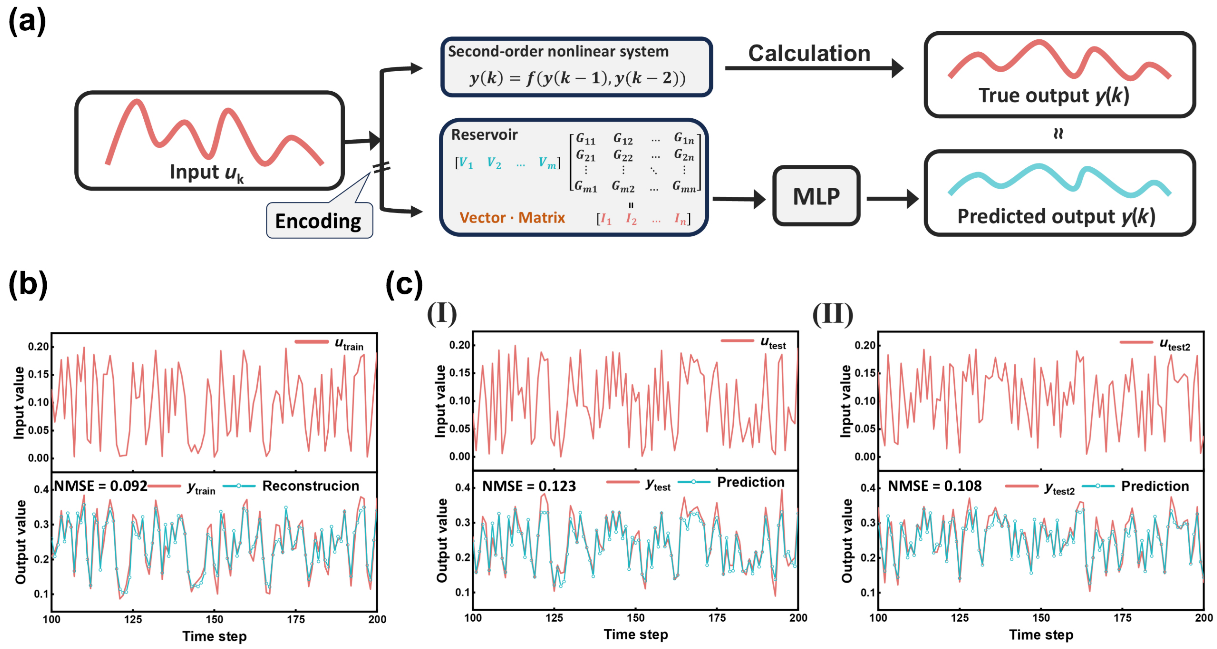

Figure 8 Solving the second-order nonlinear system task. (a) Schematic of reservoir computing for solving the second-order nonlinear system task. (b) The upper part shows the random signal input during the training process, while the lower part shows a comparison between the actual output and the predicted output from the training set. (c) (I) and (II) respectively show the random signal input (upper part) and the comparison between actual outputs and predicted outputs from the test set during two testing processes (lower part).

predictions of second-order nonlinear dynamics, demonstrating that the inherent "forgetting" window of volatile devices offers a natural advantage in time-series data processing. Overall, this study provides a comprehensive material-mechanism-application paradigm for multifunctional volatile memristors, offering new insights for brain-inspired computing hardware.

4 Experimental section

The preparation and testing of the ATA memristor were conducted at room temperature. A commercial ITO glass substrate was ultrasonically cleaned with isopropanol and deionized water, then dried with nitrogen. In an electron beam evaporation system with a base pressure of < 10^{-5} Torr, 50 nm of Al_2O_3, 5 nm of Ti, and 50 nm of Al_2O_3 were sequentially deposited, with deposition rates of 0.04 Å/s for Al_2O_3 and 0.03 Å/s for Ti. Subsequently, 145 nm of Ag was evaporated at a rate of 0.12 Å/s using a stainless-steel mask, forming the Ag/Al_2O_3/Ti/Al_2O_3/ITO vertical stack. The entire process was performed without annealing to avoid damaging the partially oxidized Ti layer (the electrical characteristics of the annealed device are provided in Note S7 in the ESM). The device cross-section was prepared using a Thermo Fisher Helios 5 CX focused ion beam–field emission scanning electron microscope. HAADF-STEM, EDS, and HRTEM images were collected using a 200 kV Talos F200X G2 cold field emission transmission electron microscope from the same manufacturer. The chemical valence states were determined using a Thermo Scientific K-Alpha XPS (Al Kα, 20 eV pass energy, calibrated to C 1s = 284.8 eV). All electrical measurements were performed on a Keithley 4200A-SCS system equipped with a probe station.

Electronic Supplementary Material: Supplementary material (HAADF image and EDS, conductive mechanism analysis of memristors, mechanism modeling of memristors, separable states of different devices, image recognition task comparison, electrical performance of devices after annealing) is available in the online version of this article at https://doi.org/10.26599/NR.2026.94908641.

Data availability

All data needed to support the conclusions in the paper are presented in the manuscript and the Electronic Supplementary Material. Additional data related to this paper may be requested from the corresponding author upon request.

Acknowledgements

This work was supported by the Graduate Student Scientific Research and Innovation Project of Ningbo University, Natural Science Foundation of Ningbo Municipality (No. 2023J007), Ningbo Municipal Science and Technology Innovation Yongjiang 2035 Key R&D Plan (No. 2025Z086), and Natural Science Foundation of Zhejiang Province (No. LDT23F05015F05).

Declaration of competing interest

All the contributing authors report no conflict of interests in this work.

Author contribution statement

J. L.: Conceptualization, methodology, experimental design, investigation, data curation, formal analysis, validation, visualization, writing – original draft, writing – review & editing. K. X. W.: Investigation, formal analysis, validation. H. Y. L.: Software, visualization. Z. Y. X.: Investigation, data curation. J. X. Z.: Formal analysis, visualization. Y. W.: Data curation. J. Y. W.: Investigation. X. Y. C.: Data curation. W. T. X.: Resources. Y. G. L.: Supervision, resources, writing – review & editing. R. J.: Conceptualization, supervision, funding acquisition, project administration, writing – review & editing. All the authors have approved the final manuscript.

Use of AI statement

None.

References

[1] Muir, D. R.; Sheik, S. The road to commercial success for neuromorphic technologies. *Nat. Commun.* **2025**, *16*, 3586.

[2] Boybat, I.; Le Gallo, M.; Nandakumar, S. R.; Moraitis, T.; Parnell, T.; Tuma, T.; Rajendran, B.; Leblebici, Y.; Sebastian, A.; Eleftheriou, E. Neuromorphic computing with multi-memristive synapses. *Nat. Commun.* **2018**, *9*, 2514.

[3] Zolfagharinejad, M.; Alegre-Ibarra, U.; Chen, T.; Kinge, S.; van der Wiel, W. G. Brain-inspired computing systems: A systematic literature review. *Eur. Phys. J. B* **2024**, *97*, 70.

[4] Stuart, G. J.; Spruston, N. Dendritic integration: 60 years of progress. *Nat. Neurosci.* **2015**, *18*, 1713–1721.

[5] Zucker, R. S.; Regehr, W. G. Short-term synaptic plasticity. *Annu. Rev. Physiol.* **2002**, *64*, 355–405.

[6] Bitterman, M. E. Classical conditioning since Pavlov. *Rev. Gen. Psychol.* **2006**, *10*, 365–376.

[7] Sumi, T.; Yamamoto, H.; Katori, Y.; Ito, K.; Moriya, S.; Konno, T.; Sato, S.; Hirano-Iwata, A. Biological neurons act as generalization filters in reservoir computing. *Proc. Natl. Acad. Sci. USA* **2023**, *120*, e2217008120.

[8] Christensen, D. V.; Dittmann, R.; Linares-Barranco, B.; Sebastian, A.; Le Gallo, M.; Redaelli, A.; Slesazeck, S.; Mikolajick, T.; Spiga, S.; Menzel, S. et al. 2022 roadmap on neuromorphic computing and engineering. *Neuromorph. Comput. Eng.* **2022**, *2*, 022501.

[9] Mehonic, A.; Ielmini, D.; Roy, K.; Mutlu, O.; Kvatinsky, S.; Serrano-Gotarredona, T.; Linares-Barranco, B.; Spiga, S.; Savel'ev, S.; Balanov, A. G. et al. Roadmap to neuromorphic computing with emerging technologies. *APL Mater.* **2024**, *12*, 109201.

[10] Kutluyarov, R. V.; Zakoyan, A. G.; Voronkov, G. S.; Grakhova, E. P.; Butt, M. A. Neuromorphic photonics circuits: Contemporary review. *Nanomaterials* **2023**, *13*, 3139.

[11] Du, C.; Cai, F. X.; Zidan, M. A.; Ma, W.; Lee, S. H.; Lu, W. D. Reservoir computing using dynamic memristors for temporal information processing. *Nat. Commun.* **2017**, *8*, 2204.

[12] Muñoz-Martin, I.; Bianchi, S.; Hashemkhani, S.; Pedretti, G.; Melnic, O.; Ielmini, D. A brain-inspired homeostatic neuron based on phase-change memories for efficient neuromorphic computing. *Front. Neurosci.* **2021**, *15*, 709053.

[13] Sun, Y. L.; Wang, H. P.; Xie, D. Recent advance in synaptic plasticity modulation techniques for neuromorphic applications. *Nano-Micro Lett.* **2024**, *16*, 211.

[14] An, Y. S.; Kim, D.; Park, Y. R.; Eo, J. S.; Kim, M.; Kim, D.; Kim, H. B.; Lee, B.; Wang, G. Implementation of monolithic 3D integrated TiO_x memristor-based neural network for high-performance in-memory computing. *Nano Energy* **2025**, *139*, 110999.

[15] Ielmini, D.; Pedretti, G. Resistive switching random-access memory (RRAM): Applications and requirements for memory and computing. *Chem. Rev.* **2025**, *125*, 5584–5625.

[16] Kim, S. J.; Lee, H. J.; Lee, C. H.; Jang, H. W. 2D materials-based 3D integration for neuromorphic hardware. *npj 2D Mater. Appl.* **2024**, *8*, 70.

[17] Schranghamer, T. F.; Oberoi, A.; Das, S. Graphene memristive synapses for high precision neuromorphic computing. *Nat. Commun.* **2020**, *11*, 5474.

[18] Yang, Z.; Yue, W. S.; Liu, C.; Tao, Y. Y.; Tiw, P. J.; Yan, L. H.; Yang, Y. X.; Zhang, T.; Dang, B. J.; Liu, K. Q. et al. Fully hardware memristive neuromorphic computing enabled by the integration of trainable dendritic neurons and high-density RRAM chip. *Adv. Funct. Mater.* **2024**, *34*, 2405618.

[19] Zhang, X. L.; Ji, H.; Jiang, R. Asymmetric-structure-induced self-rectifying in nanoscale HfO_2-based RRAM array. *IEEE Trans. Electron Devices* **2019**, *66*, 3337–3341.

[20] Bisquert, J.; Shim, W.; Kim, S. Y.; Linares-Barranco, B. Synaptic function in memristor devices for neuromorphic circuit applications. *Adv. Electron. Mater.* **2025**, *11*, 2400903.

[21] Kim, D.; Jeon, B.; Lee, Y.; Kim, D.; Cho, Y.; Kim, S. Prospects and applications of volatile memristors. *Appl. Phys. Lett.* **2022**, *121*, 010501.

[22] Moon, T.; Soh, K.; Kim, J. S.; Kim, J. E.; Chun, S. Y.; Cho, K.; Yang, J. J.; Yoon, J. H. Leveraging volatile memristors in neuromorphic computing: From materials to system implementation. *Mater. Horiz.* **2024**, *11*, 4840–4866.

[23] Messaris, I.; Ascoli, A.; Demirkol, A. S.; Ntinas, V.; Prousalis, D.; Tetzlaff, R. High frequency response of volatile memristors. *Adv. Electron. Mater.* **2024**, *10*, 2400172.

[24] Wang, Y. Z.; Wang, W.; Xu, H.; Liu, S.; Cao, R. R.; Sun, Y.; Tong, P. W.; Song, B.; Li, Q. J. Nanolayered NbO_2-based dynamic memristor for leaky integrate and fire neuron. *ACS Appl. Nano Mater.* **2024**, *7*, 10679–10689.

[25] Yi, W.; Tsang, K. K.; Lam, S. K.; Bai, X. W.; Crowell, J. A.; Flores, E. A. Biological plausibility and stochasticity in scalable VO_2 active memristor neurons. *Nat. Commun.* **2018**, *9*, 4661.

[26] Ju, D.; Noh, M.; Lee, S.; Kim, G.; Park, J.; Kim, S. Self-rectifying volatile memristor for highly dynamic functions. *Adv. Funct. Mater.* **2025**, *35*, 2423880.

[27] Kim, D.; Shin, J.; Kim, S. Implementation of reservoir computing using volatile WO*x*-based memristor. *Appl. Surf. Sci.* **2022**, *599*, 153876.

[28] Mahata, C.; Kang, M.; Kim, S. Multi-level analog resistive switching characteristics in tri-layer $HfO_2/Al_2O_3/HfO_2$ based memristor on ITO electrode. *Nanomaterials* **2020**, *10*, 2069.

[29] Park, S.; Spetzler, B.; Ivanov, T.; Ziegler, M. Multilayer redox-based $HfO_x/Al_2O_3/TiO_2$ memristive structures for neuromorphic computing. *Sci. Rep.* **2022**, *12*, 18266.

[30] Park, J.; Kumar, A.; Zhou, Y. C.; Oh, S.; Kim, J. H.; Shi, Y. H.; Jain, S.; Hota, G.; Qiu, E. B.; Nagle, A. L. et al. Multi-level, forming and filament free, bulk switching trilayer RRAM for neuromorphic computing at the edge. *Nat. Commun.* **2024**, *15*, 3492.

[31] Olson, D. H.; Freedy, K. M.; McDonnell, S. J.; Hopkins, P. E. The influence of titanium adhesion layer oxygen stoichiometry on thermal boundary conductance at gold contacts. *Appl. Phys. Lett.* **2018**, *112*, 171602.

[32] Di Martino, G.; Demetriadou, A.; Li, W. W.; Kos, D.; Zhu, B. N.; Wang, X. J.; de Nijs, B.; Wang, H. Y.; MacManus-Driscoll, J.; Baumberg, J. J. Real-time *in situ* optical tracking of oxygen vacancy migration in memristors. *Nat. Electron.* **2020**, *3*, 687–693.

[33] Menzel, S.; Waters, M.; Marchewka, A.; Böttger, U.; Dittmann, R.; Waser, R. Origin of the ultra-nonlinear switching kinetics in oxide-based resistive switches. *Adv. Funct. Mater.* **2011**, *21*, 4487–4492.

[34] Pereda, A. E. Electrical synapses and their functional interactions with chemical synapses. *Nat. Rev. Neurosci.* **2014**, *15*, 250–263.

[35] Ruiz Puigdollers, A.; Schlexer, P.; Tosoni, S.; Pacchioni, G. Increasing oxide reducibility: The role of metal/oxide interfaces in the formation of oxygen vacancies. *ACS Catal.* **2017**, *7*, 6493–6513.

[36] Jeong, D. S.; Cheong, B. K.; Kohlstedt, H. $Pt/Ti/Al_2O_3/Al$ tunnel junctions exhibiting electroforming-free bipolar resistive switching behavior. *Solid-State Electron.* **2011**, *63*, 1–4.

[37] Filatova, E. O.; Konashuk, A. S.; Sakhonenkov, S. S.; Sokolov, A. A.; Afanas'ev, V. V. Re-distribution of oxygen at the interface between γ-Al_2O_3 and TiN. *Sci. Rep.* **2017**, *7*, 4541.

[38] Li, W. T.; Tuo, Y.; Mi, W.; Wang, D.; Wang, M.; Zhou, L. W.; Zhao, J. S. The effect of oxygen affinity electrode Ti on the performance of vanadium oxide-based valence change resistive random access memory. *Vacuum* **2023**, *209*, 111794.

[39] Winter, R.; Shekhter, P.; Tang, K. C.; Floreano, L.; Verdini, A.; McIntyre, P. C.; Eizenberg, M. Effects of titanium layer oxygen scavenging on the high-*k*/InGaAs interface. *ACS Appl. Mater. Interfaces* **2016**, *8*, 16979–16984.

[40] Qahtan, T. F.; Owolabi, T. O.; Saleh, T. A. X-ray photoelectron spectroscopy of surface-treated TiO_2 mesoporous film by 500 eV argon ion beam. *J. Mol. Liq.* **2024**, *393*, 123556.

[41] Davis, B. E.; Strandwitz, N. C. Dependence of the metal-insulator-semiconductor Schottky barrier height on insulator composition. *ACS Appl. Electron. Mater.* **2024**, *6*, 770–776.

[42] Fu, T. D.; Fu, S.; Sun, L.; Gao, H. Y.; Yao, J. An effective sneak-path solution based on a transient-relaxation device. *Adv. Mater.* **2023**, *35*, 2207133.

[43] Park, S. O.; Jeong, H.; Park, J.; Bae, J.; Choi, S. Experimental demonstration of highly reliable dynamic memristor for artificial neuron and neuromorphic computing. *Nat. Commun.* **2022**, *13*, 2888.

[44] Weilenmann, C.; Ziogas, A. N.; Zellweger, T.; Portner, K.; Mladenović, M.; Kaniselvan, M.; Moraitis, T.; Luisier, M.; Emboras, A. Single neuromorphic memristor closely emulates multiple synaptic mechanisms for energy efficient neural networks. *Nat. Commun.* **2024**, *15*, 6898.

[45] Wang, Y. C.; Zheng, J. W.; Shang, Y. Y.; Guo, D. Y.; Wang, H. X.; An, Z. Y.; Chen, X. C.; Huang, R. X.; Jiang, J. Y.; Sun, K. et al. LTP-LTD transformation of unipolar pulse voltage-driven zinc oxide memristors via TiO_2 thin layer incorporation. *J. Mater. Chem. C* **2024**, *12*, 1281–1288.

[46] Kim, S.; Choi, S.; Lu, W. Comprehensive physical model of dynamic resistive switching in an oxide memristor. *ACS Nano* **2014**, *8*, 2369–2376.

[47] Zhong, X. L.; Rungger, I.; Zapol, P.; Nakamura, H.; Asai, Y.; Heinonen, O. The effect of a Ta oxygen scavenger layer on HfO_2-based resistive switching behavior: Thermodynamic stability, electronic structure, and low-bias transport. *Phys. Chem. Chem. Phys.* **2016**, *18*, 7502–7510.

[48] Ji, J. P.; Gao, D. C.; Wu, H. Y.; Xiong, M.; Stajkovic, N.; Latte Bovio, C.; Yang, C. Y.; Santoro, F.; Tu, D. Y.; Fabiano, S. Single-transistor organic electrochemical neurons. *Nat. Commun.* **2025**, *16*, 4334.

[49] Lu, J.; Xiang, Z. Y.; Wang, K. X.; Wang, Z. Y.; Shi, S.; Liu, Z. M.; Chen, X. R.; Hu, X. Y.; Jiang, R. Frequency synaptic behavior of ZnO/HfZrO memristor with pulsed stimuli. *Appl. Phys. Lett.* **2024**, *125*, 083508.

[50] Du, N.; Zhao, X. Y.; Chen, Z. A.; Choubey, B.; Di Ventra, M.; Skorupa, I.; Bürger, D.; Schmidt, H. Synaptic plasticity in memristive artificial synapses and their robustness against noisy inputs. *Front. Neurosci.* **2021**, *15*, 660894.

[51] Wang, W. X.; Wang, Y. Q.; Yin, F. F.; Niu, H. S.; Shin, Y. K.; Li, Y.; Kim, E. S.; Kim, N. Y. Tailoring classical conditioning behavior in TiO_2 nanowires: ZnO QDs-based optoelectronic memristors for neuromorphic hardware. *Nano-Micro Lett.* **2024**, *16*, 133.

[52] Zhang, G. H.; Qin, J. R.; Zhang, Y.; Gong, G. D.; Xiong, Z. Y.; Ma, X. Y.; Lv, Z. Y.; Zhou, Y.; Han, S. T. Functional materials for memristor-based reservoir computing: Dynamics and applications. *Adv. Funct. Mater.* **2023**, *33*, 2302929.

[53] Chen, Z. W.; Li, W. J.; Fan, Z.; Dong, S.; Chen, Y. H.; Qin, M. H.; Zeng, M.; Lu, X. B.; Zhou, G. F.; Gao, X. S. et al. All-ferroelectric implementation of reservoir computing. *Nat. Commun.* **2023**, *14*, 3585.

[54] Abu-Dakka, F. J.; Saveriano, M. Variable impedance control and learning-a review. *Front. Robot. AI* **2020**, *7*, 590681.

[55] Sanchez-Todo, R.; Bastos, A. M.; Lopez-Sola, E.; Mercadal, B.; Santarnecchi, E.; Miller, E. K.; Deco, G.; Ruffini, G. A physical neural mass model framework for the analysis of oscillatory generators from laminar electrophysiological recordings. *NeuroImage* **2023**, *270*, 119938.

[56] Moon, S.; Park, C.; Jung, Y.; Min, K. S.; Ko, H.; Yoon, T. S. Reservoir computing determined by nonlinear weight dynamics in Gd-doped CeO_2/CeO_2 bi-layered oxide memristors. *J. Mater. Chem. C* **2025**, *13*, 4894–4909.

[57] Hülser, T.; Köster, F.; Lüdge, K.; Jaurigue, L. Deriving task specific performance from the information processing capacity of a reservoir computer. *Nanophotonics* **2023**, *12*, 937–947.

[58] Lee, S. H.; Kim, S.; Han, J.; Shim, S. K.; Son, K.; Shin, D. H.; Jeong, H.; Park, J.; Shin, S. J.; Jang, Y. H. et al. Electrically tunable physical reservoir computing on two-terminal devices. *npj Unconv. Comput.* **2025**, *2*, 27.